

MATERIALS SCIENCE

Electron microscopy of nanoparticle superlattice formation at a solid-liquid interface in nonpolar liquids

E. Cepeda-Perez^{1*†}, D. Doblas^{1*‡}, T. Kraus^{1,2§}, N. de Jonge^{1,3§}

Nanoparticle superlattice films form at the solid-liquid interface and are important for mesoscale materials, but are notoriously difficult to analyze before they are fully dried. Here, the early stages of nanoparticle assembly were studied at solid-liquid interfaces using liquid-phase electron microscopy. Oleylamine-stabilized gold nanoparticles spontaneously formed thin layers on a silicon nitride (SiN) membrane window of the liquid enclosure. Dense packings of hexagonal symmetry were obtained for the first monolayer independent of the nonpolar solvent type. The second layer, however, exhibited geometries ranging from dense packing in a hexagonal honeycomb structure to quasi-crystalline particle arrangements depending on the dielectric constant of the liquid. The complex structures formed by the weaker interactions in the second particle layer were preserved, while the surface remained immersed in liquid. Fine-tuning the properties of the involved materials can thus be used to control the three-dimensional geometry of a superlattice including quasi-crystals.

INTRODUCTION

Nanoparticle superlattices are regular arrays of densely packed nanoparticles in two or three dimensions (1). They combine the particles into new mesoscale materials; for example, semiconductor particle superlattices act as “meta”—semiconductors that can be doped with particles (2–4). Plasmonic particles in dense superlattices couple and form collective modes with angle-dependent, tunable wavelength responses (5). Large electric fields occur in the gaps between these particles; metal nanoparticles are used to surface-enhanced Raman spectrometry (6). In catalysis, superlattices provide adjacent active sites and gaps that can act as hotspots and are tuned for specific reactions (7). Superlattices have been formed at liquid-liquid (8), gas-liquid (2), and solid-liquid interfaces (9). Although predicting superlattice structure remains difficult, it is clear that the structure depends on particle-substrate, particle-particle, and particle-liquid interactions, both static and dynamic. Simulation of the multiple stages of superlattice assembly is yet to be possible, and there is very little in situ, real-space data to aid modeling. Superlattices are commonly formed by evaporating the liquid of dispersion at an interface. The first reports on the colloidal self-assembly of binary superlattices (10, 11), for example, used a solid substrate that was submerged in a volume of slowly evaporating dispersion. Others spread nanoparticle dispersions on top of an immiscible liquid to create a superlattice at the gas-liquid interface and subsequently transferred the structure onto a solid substrate (12–14). Because of limitations in methods, it has been challenging to obtain experimental insights into the fundamental mechanisms that drive superlattice formation at interfaces before the dispersion dries. Small-angle x-ray scattering (15–20) provides information about ensemble averages, while in situ optical microscopy (21–23) does not have sufficient spatial resolution to image nanoparticles.

¹INM—Leibniz Institute for New Materials, Saarbrücken, Germany. ²Colloid and Interface Chemistry, Saarland University, Saarbrücken, Germany. ³Department of Physics, Saarland University, Saarbrücken, Germany.

*These authors contributed equally to this work.

†Present address: SPECS Surface Nano Analysis, Berlin, Germany.

‡Present address: European XFEL, Schenefeld, Germany.

§Corresponding author. Email: tobias.kraus@leibniz-inm.de (T.K.); niels.dejonge@leibniz-inm.de (N.d.J.)

Here, superlattices of gold nanoparticles (AuNPs) were directly imaged while suspended in different nonpolar solvents using liquid-phase electron microscopy (LP-EM). AuNPs in the first layer above a surface strongly interact both with the substrate and with each other. However, once a super structure assembles layer by layer, the interactions with the surface diminish, and the patterns are subjected to weaker forces between the nanoparticles that are mediated by the liquid properties. To study this transition from strong particle-surface interactions to weaker interparticle interactions, we examined the patterns of a monolayer and of a double layer under different solvent conditions. In particular, the formation of superlattices was studied originating from a single type of oleylamine-coated AuNPs assembled on a silicon nitride (SiN) membrane. The interactions between AuNPs and substrate were varied by changing the solvent. We used scanning transmission electron microscopy (STEM) to obtain the highest possible spatial resolution for the lowest possible electron flux so as to minimize influencing the sample by the probe method (24, 25).

RESULTS

AuNP films examined at the solid-liquid interface with LP-EM

LP-EM was used to study the organization of layers of AuNPs at a solid-liquid interface in nonpolar liquids. The nanoparticles had a mean core diameter of 7.2 ± 0.7 nm (fig. S1) and were stabilized by a layer of oleylamine of ~2-nm thickness (26) with an estimated ligand density of 5 nm^{-2} (Fig. 1) (27). To render the surface polar, the SiN membrane was subjected to an oxidizing plasma directly before sample loading (28). LP-EM was then used to observe AuNPs located at the solid-liquid interface. To vary the range of the interactions, we tested four different nonpolar liquids with different dielectric constant (Table 1). Thin layers of AuNPs had accumulated at the SiN window for all liquids (Fig. 2, A to D). The presence of liquid during the LP-EM experiment was verified by measuring the liquid thickness (table S1). Because the samples were kept in a wet state at all times, particle-substrate interactions must have been present, which attracted the nanoparticles from the liquid to the SiN surface. The particles formed thin film rather than compact of fractal aggregates (Fig. 2, A to D), which excludes agglomeration in bulk followed by adsorption on the substrate.

Copyright © 2020
The Authors, some
rights reserved;
exclusive licensee
American Association
for the Advancement
of Science. No claim to
original U.S. Government
Works. Distributed
under a Creative
Commons Attribution
NonCommercial
License 4.0 (CC BY-NC).

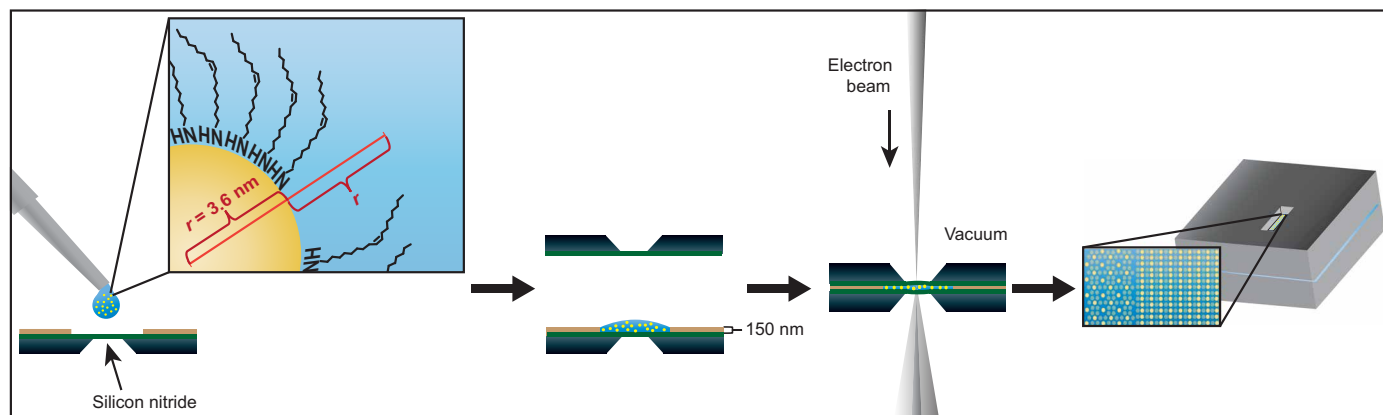


Fig. 1. Schematic of representation of LP-EM of oleylamine-capped AuNPs in nonpolar liquids. From left to right: Schematic of the assembled liquid cell. A droplet of AuNPs is placed on a microchip with a thin SiN membrane window and containing a spacer of 150-nm thickness, after which a liquid cell is assembled using a second microchip. Images are obtained by scanning the electron beam over the sample and recording transmitted electrons, whereby the liquid is protected from evaporation by the SiN membrane window. Data of self-assembled nanoparticles are then analyzed.

Table 1. Geometries observed for different solvents. Information about regular structures of nanoparticle films that spontaneously formed on polar Si_3N_4 in different solvents as derived from liquid-phase electron micrographs. Values are indicated for the solvent's dielectric constant ϵ_r .

Solvent	ϵ_r	Symmetry in single layers	Symmetry in double layers
Toluene	2.38	Hexagonal	Quasi-crystal, dodecagonal
Hexadecane	2.09	Hexagonal	Cubic (body-centered cubic)
Cyclohexane	2.02	Hexagonal	Hexagonal
Octane	2.00	Hexagonal	Cubic

Most of the surface areas shown in Fig. 2 seem to be covered with a layer of AuNPs. The overall densities were the highest for the linear-chain solvents (Fig. 2, A and B), while net-like structures with holes in the film were observed for the cyclic solvents (Fig. 2, C and D), in which the surface was not covered with nanoparticles. The observation of locally dense films with holes indicates that the lateral interparticle interactions also contribute to film deposition. A hole in the film can then be explained by a combination of a limited surface density of nanoparticles and an effective attraction between the nanoparticles. Similar patterns were reported by Ge and Brus (29), who liken their formation mechanism to spinodal dewetting of liquids on solids.

Hexagonal patterns observed for monolayers of AuNPs

The assembled AuNPs layers were imaged at higher magnification to investigate the presence of regular structures/patterns. Hexagonal, dense packings occurred for monolayer areas in hexadecane (Fig. 3A), as verified by a fast Fourier transform (FFT). The measured signal in such a patch varied between two discrete levels (Fig. 3B): a peak signal at the location of a nanoparticle and the signal level of the background in between. Thus, the patch likely presents a monolayer. Similar hexagonal patterns were also observed for monolayers of AuNP obtained in the other solvents (figs. S2 and S3), and the measured center-to-center distance between adjacent nanoparticles in

all solvents was around 11 ± 1 nm, consistent with densely packed AuNPs of a diameter of 7.2 ± 0.7 nm with the applied coating of 2-nm thickness. Therefore, it is assumed that the combination of strong particle-substrate interactions and weaker lateral particle-particle attraction leads to dense packing that is only weakly affected by the solvent choice. An additional eight different sample areas were analyzed. In four of these areas, patches with hexagonal symmetry were observed, while others contained either areas with sparsely distributed particles or multiple layers.

Cubic arrangements observed for double layers of AuNP in linear solvents

Several areas of the AuNP layer in hexadecane had brighter and fainter spots, indicating the presence of AuNPs on top of a monolayer (Fig. 4A). The signal in the image exhibited three discrete levels (Fig. 4B). The structure of the top layer deviated from dense packing; for example, the FFT of the pattern in Fig. 4A shows a cubic structure with typical particle spacings of 14 and 7 nm. Note that the AuNPs appear to be “melted” together and clear boundaries are not visible between some of the AuNPs. This lack of visible boundaries is the result of the limited signal-to-noise ratio obtained while imaging the AuNPs in the liquid layer at the lowest possible electron dose. The AuNPs are suggested to have been ordered in a two-layer structure on the basis of a body-centered cubic structure with a theoretical edge length of 8.3 nm (see schematic model drawn in Fig. 4, B and C). The observed patterns remained stable also after recording additional images at the same sample area in time-lapse series (see movie S1). Patches of cubic symmetry were observed in a further four investigated sample regions, essentially all regions containing multiple layers (data not shown). Cubic arrangements were also found for non-monolayer areas in octane (fig. S3).

Different arrangements observed for double layers of AuNP in cyclic solvents

The cyclic solvents caused a different ordering of the second particle layer. Cyclohexane led to a dense, hexagonal top layer packed on top and of the same spacings as the bottom layer (Fig. 5A). The density of the top particle layers was much reduced in toluene, the solvent with the highest dielectric constant ($\epsilon_{\text{Toluene}} \approx 2.38$), while all other

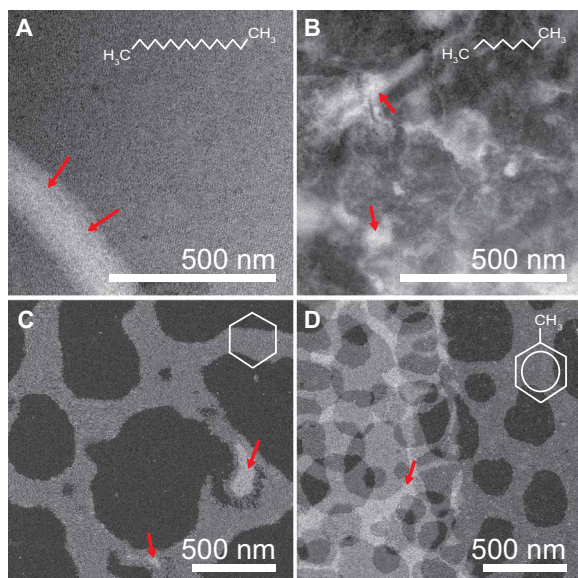


Fig. 2. AuNPs films formed in liquid at the interface with a SiN membrane. Exemplary STEM images observed in different nonpolar liquids: (A) hexadecane (liquid thickness $l_{\text{solv}} = 3.9 \mu\text{m}$, electron flux $D = 1.3 \text{ e}^-/\text{s}\text{\AA}^2$), (B) octane ($l_{\text{solv}} = 6.9 \mu\text{m}$, $D = 0.3 \text{ e}^-/\text{s}\text{\AA}^2$), (C) cyclohexane ($l_{\text{solv}} = 2.3 \mu\text{m}$, $D = 0.3 \text{ e}^-/\text{s}\text{\AA}^2$), and (D) toluene ($l_{\text{solv}} = 1.0 \mu\text{m}$, $D = 0.3 \text{ e}^-/\text{s}\text{\AA}^2$).

solvents had $\epsilon \approx 2$. Structures were found with a hexagonal base and a so-called rhombitrihexagonal tiling (Fig. 5B) characterized by one triangle, two parallelograms, and one hexagon on each vertex (Fig. 5C) (30). Some regions had hexagonal symmetry (see FFT of Fig. 5D) but no translational periodicity. The arrangement resembled a non-self-similar modification of the so-called bronze-mean hexagonal quasi-crystal (BMQC) (Fig. 5, D and E) (31). The modification was composed of three types of tiles based on small (s) and large (l) equilateral triangles and rectangles whose dimension is given by the edge of the small and large triangles ($s \times l$) (Fig. 5F) (31). The model in Fig. 5 (E and F) shows small triangles with side lengths of 2 nm and large triangles with side lengths of 10 nm that match our structures. Patches of quasi-crystalline nature were also found at other sample areas (fig. S5).

In contrast to the linear solvents, the second particle layer was unstable under prolonged electron beam irradiation, indicating a weaker bonding of the particles of the second layer compared to those of the first layer (see movie S2). The first five consecutive images recorded at the same location were identical, after which changes in the pattern became visible. The electron dose of the first image was thus sufficiently small to observe the pattern before the electron beam irradiation led to the disassembly of the second layer.

DISCUSSION

The reduced density of the particle packings above the bottom monolayer is presumably due to the decay of the particle-substrate interaction potential. If it is assumed that the highly polar substrate induces dipoles in the particles, the resulting Debye attraction for particles with diameter at a distance from the substrate should approximately with (32)

$$U \propto -\left(\frac{a}{h} + \frac{a}{h+2a} + \ln\left(\frac{h}{h+2a}\right)\right) \quad (1)$$

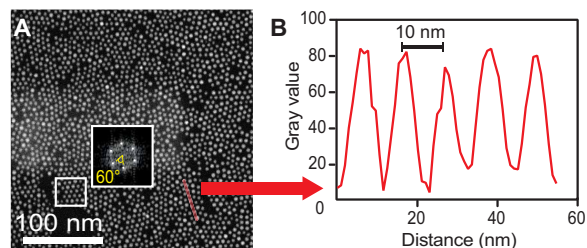


Fig. 3. Single layers of AuNP at the solid-liquid interface in hexadecane. (A) STEM image of a single layer of AuNPs. The inset corresponds to the FFT: $l_{\text{solv}} = 3.9 \mu\text{m}$, $D = 5.0 \text{ e}^-/\text{s}\text{\AA}^2$. (B) Plot of the gray value versus position acquired for the red line shown in (A).

The particle-substrate attraction in the first layer will then exceed those in the second layer by a factor of 27 if it is dominated by gold cores that have a diameter of 7.2 nm and have centers that are 2 and 13 nm above the substrate in the first and second layers, respectively. Note that this is a rough estimate that does not consider possible deviations of the nanoscale particles from bulk properties.

Quasi-crystal packings can form when particles interact with certain specific potentials and are considered as a second well-ordered form of matter (33). Dotera *et al.* (31) showed that a potential with a hard core and a softer square shoulder with a shoulder-to-core ratio λ can lead to the formation of a self-similar BMQC for $\lambda \sim 2.186$. If it is assumed that the potentials between the AuNPs used can be described with a similar hard-core/square-shoulder model, and that the hard core of the nanoparticles used is surrounded by a soft monolayer of toluene molecules (0.58 nm thick) (34), the resulting shoulder-to-core ratio is $\lambda = 1.7$. The ratio l/s of the self-similar BMQC (31) is ~ 1.330 , while we found $l/s = 5$ (Fig. 5, E and F). We conclude that the AuNPs in our experiment form a non-self-similar modification of the BMQC, possibly along similar mechanisms as suggested by Dotera *et al.* (31).

Solvents with high dielectric constants reduced packing densities and enabled the formation of quasi-crystalline structures. This is consistent with our hypothesis of substrate-induced self-assembly with additional lateral particle-particle attraction. The hexagonal packing of the bottom layer in all liquids indicates strong attraction either between neighboring particles or between particles and the substrate. Because the particle-particle interactions should not depend on the particle-substrate spacing, the reduced density of the top layer suggests a strong role of particle-substrate attraction. These are likely Debye attraction (see above) that also explains the reduced density of the top particle layers in solvents with a high dielectric constant, ϵ : The interaction potential between a permanent dipole in the surface and an induced dipole in the particle scales with $U_{\text{Debye}} \propto \epsilon^{-2}$ and is thus 28% weaker in toluene than in cyclohexane.

The particle-substrate interactions are expected to be unspecific and cannot cause quasi-crystalline or other low-density packings. However, they enable self-assembly by providing a driving force that moves the particles toward the surface. Strongly attractive particle-substrate interactions should lead to a maximally dense, minimum-energy hexagonal arrangement of the layer, unless the attraction is strong enough to suppress lateral motion of the particles, thus causing a jamming-limited geometry.

The hexagonal order that we observe in the bottom particle layers is consistent with strong interactions between substrate and particles, where the particles retain some mobility but pack densely. Lateral

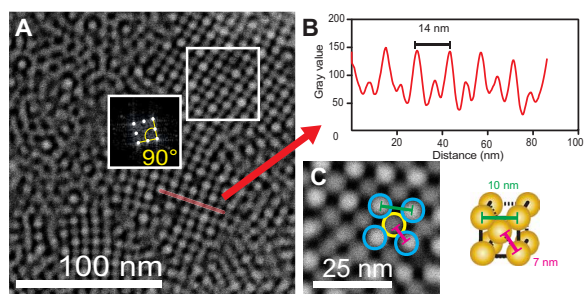


Fig. 4. Self-assembled multi-layer structures in hexadecane. (A) Double layer of AuNPs at the interface between the SiN membrane with the corresponding FFT in the inset: $I_{\text{solv}} = 2.1 \mu\text{m}$, $D = 30.4 \text{ e}^-/\text{s}\text{\AA}^2$. (B) Plot of the gray value versus position acquired for the red line in (A) showing the presence of two layers of nanoparticles. (C) Digital zoom of the region shown in (A) and its corresponding body-centered cubic model.

particle arrangements, depending on the strength of the dielectric constant of the liquid. The complex structures formed by the weaker interactions in the second particle layer were preserved, while the surface remained immersed in liquid. It is thus possible to control the three-dimensional geometry of a superlattice of a metamaterial including complex quasi-crystalline structures by fine-tuning the properties of the involved liquid and the involved nanoparticles, as well as interface material.

MATERIALS AND METHODS

Synthesis and characterization of oleylamine-capped AuNPs

All chemicals used for the synthesis of the nanoparticles were purchased from Sigma-Aldrich and used without further purification. Oleylamine-capped AuNPs with a mean radius of 3.6 nm were synthesized via the reduction of HAuCl_4 by an amine-borane complex in the presence of oleylamine following the route reported by Wu *et al.* (20). The resulting particles were isolated by repeated centrifugation and dispersed in octane, hexadecane, cyclohexane, or toluene.

Liquid-phase STEM

A liquid flow TEM holder (Poseidon, Protochips Inc., NC, USA) was used to image the nanoparticles in different solvents. Liquid-phase STEM experiments were carried out using a transmission electron microscope equipped with a cold field emission gun (JEM-ARM 200F, JEOL, Japan) and a STEM probe corrector (CEOS GmbH, Germany). The electron beam energy was 200 keV. The annular dark-field (ADF) detector was used with a camera length of 8 cm, an aperture of 30 μm , and a 5C probe, resulting in a detector opening semi-angle of 43 mrad reflecting the active areas of the detector. The electron probe current I_p was 80 pA. The image series was acquired with a pixel dwell time of $\tau = 1 \mu\text{s}$ and an image size of 512×512 pixels. Depending on the magnification, the pixel size was either $s = 1.3, 0.48, \text{ or } 0.39 \text{ nm}$. The acquisition time between two consecutive recordings amounted to $v = 1.08 \text{ s}$. The electron flux, D , expressed in electrons per unit area per unit time was calculated from $D = \tau^* I_p / (v^* e^* s^2)$, where e is the elementary charge.

Low-dose electron microscopy

To limit electron beam exposure of the sample as much as possible, the STEM data acquisition was accomplished using a low-dose procedure. For a new sample, the focus and stigmator were first adjusted. The beam current density passing through the sample was measured for determining the liquid thickness (see table S1). The beam was then blanked, and the stage was moved to a sample area that had not been exposed before to the electron beam. The blanker was then opened, and immediately, the recording of either a single image or a movie was immediately started. The first image was always used for the images shown. This image was thus exposed to the electron beam during $v = 1.08 \text{ s}$. The total electron dose for the images shown thus follows from D^*v . The beam was then blanked, and the stage was moved to a new position for the acquisition of data at another unexposed location.

Image processing

Gray value line scan plots were obtained using the Analyze>Plot profile command of ImageJ (National Institutes of Health). The FFT was obtained by selecting an area of the ADF-STEM still and using the Process>FFT command of ImageJ.

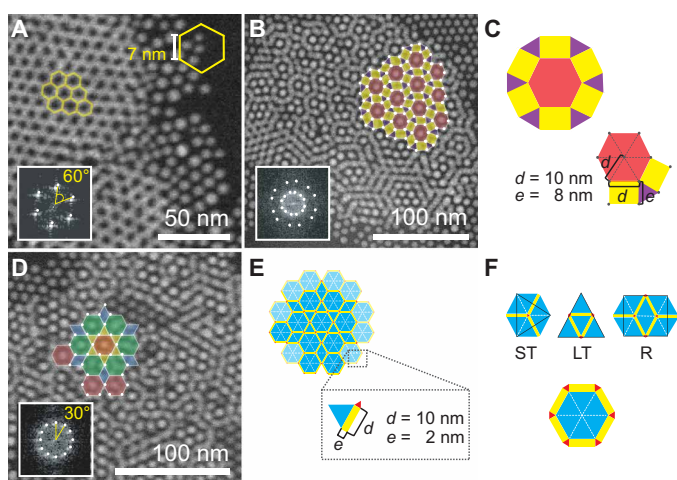


Fig. 5. Crystal and quasi-crystal AuNP structures self-assembled at a solid-liquid interface. (A) Hexagonal lattice observed for AuNPs in cyclohexane: $I_{\text{solv}} = 0.5 \mu\text{m}$, $D = 30.4 \text{ e}^-/\text{s}\text{\AA}^2$. (B) AuNPs in toluene arranged in a rhombitrihexagonal pattern (colored area): $I_{\text{solv}} = 0.8 \mu\text{m}$, $D = 30.4 \text{ e}^-/\text{s}\text{\AA}^2$. (C) Schematic of rhombitrihexagonal tiles. The dimensions found for the triangles, parallelograms, and hexagons (each side) were 8.3 nm, 8.3 nm by 10 nm, and 10 nm, respectively. (D) AuNPs in toluene arranged in a non-self-similar modification of the BMQC (colored area) ($I_{\text{solv}} = 0.8 \mu\text{m}$, $D = 30.4 \text{ e}^-/\text{s}\text{\AA}^2$). (E) Dimensions of the non-self-similar BMHC, and (F) its tiles and fundamental dodecagon symmetry.

interactions cause less dense packings in the layers that are further removed from the substrate. The strength of the lateral interactions depends on the solvent; they may include nonadditive collective particle interactions that contribute to the formation of quasi-crystalline superlattices.

The spatially resolved data obtained with LP-EM allowed us to distinguish local from global particle densities, detect different packings in AuNPs adjacent to the substrate, and examine particles assembled on top of the first assembled monolayer. The mechanism behind the formation of self-assembled superlattices of AuNPs at a solid-liquid interface gives rise to a rich variety of geometries depending on the delicate interplay between surface, particle ensemble, and liquid. Particle configurations were observed ranging from dense packing in a hexagonal honeycomb structure to quasi-crystalline

SUPPLEMENTARY MATERIALS

Supplementary material for this article is available at <http://advances.sciencemag.org/cgi/content/full/6/20/eaba1404/DC1>

REFERENCES AND NOTES

- M. A. Boles, M. Engel, D. V. Talapin, Self-assembly of colloidal nanocrystals: From intricate structures to functional materials. *Chem. Rev.* **116**, 11220–11289 (2016).
- A. G. Dong, J. Chen, P. M. Vora, J. M. Kikkawa, C. B. Murray, Binary nanocrystal superlattice membranes self-assembled at the liquid–air interface. *Nature* **466**, 474–477 (2010).
- D. V. Talapin, C. B. Murray, PbSe nanocrystal solids for n- and p-channel thin film field-effect transistors. *Science* **310**, 86–89 (2005).
- D. Vanmaekelbergh, P. Liljeroth, Electron-conducting quantum dot solids: Novel materials based on colloidal semiconductor nanocrystals. *Chem. Soc. Rev.* **34**, 299–312 (2005).
- C.-F. Chen, S.-D. Tzeng, H.-Y. Chen, K.-J. Lin, S. Gwo, Tunable plasmonic response from alkanethiolate-stabilized gold nanoparticle superlattices: Evidence of near-field coupling. *J. Am. Chem. Soc.* **130**, 824–826 (2008).
- C. Matricardi, C. Hanske, J. L. Garcia-Pomar, J. Langer, A. Mihi, L. M. Liz-Marzán, Gold nanoparticle plasmonic superlattices as surface-enhanced raman spectroscopy substrates. *ACS Nano* **12**, 8531–8539 (2018).
- E. Auyeung, W. Morris, J. E. Mondloch, J. T. Hupp, O. K. Farha, C. A. Mirkin, Controlling structure and porosity in catalytic nanoparticle superlattices with DNA. *J. Am. Chem. Soc.* **137**, 1658–1662 (2015).
- S. Shi, T. P. Russell, Nanoparticle assembly at liquid–liquid interfaces: From the nanoscale to mesoscale. *Adv. Mater.* **30**, 1800714 (2018).
- C. B. Murray, C. R. Kagan, M. G. Bawendi, Synthesis and characterization of monodisperse nanocrystals and close-packed nanocrystal assemblies. *Annu. Rev. Mater. Sci.* **30**, 545–610 (2000).
- F. X. Redl, K. S. Cho, C. B. Murray, S. O'Brien, Three-dimensional binary superlattices of magnetic nanocrystals and semiconductor quantum dots. *Nature* **423**, 968–971 (2003).
- E. V. Shevchenko, D. V. Talapin, N. A. Kotov, S. O'Brien, C. B. Murray, Structural diversity in binary nanoparticle superlattices. *Nature* **439**, 55–59 (2006).
- C. P. Collier, R. J. Saykally, J. J. Shiang, S. E. Henrichs, J. R. Heath, Reversible tuning of silver quantum dot monolayers through the metal–insulator transition. *Science* **277**, 1978–1981 (1997).
- N. A. Kotov, F. C. Meldrum, C. Wu, J. H. Fendler, Monoparticulate layer and Langmuir–Blodgett-type multiparticulate layers of size-quantized cadmium sulfide clusters: A colloid–chemical approach to superlattice construction. *J. Phys. Chem.* **98**, 2735–2738 (1994).
- X. Peng, Y. Zhang, B. Zou, L. Xiao, T. Li, J. Yang, Formation of nanoparticulate iron(III) oxide-stearate multilayer through Langmuir–Blodgett method. *J. Phys. Chem.* **96**, 3412–3415 (1992).
- M. Corricelli, D. Altamura, M. L. Curri, T. Sibillano, D. Siliqi, A. Mazzone, N. Depalo, E. Fanizza, D. Zanchet, C. Giannini, M. Striccoli, GISAXS and GIWAXS study on self-assembling processes of nanoparticle based superlattices. *CrystEngComm* **16**, 9482–9492 (2014).
- Z. Jiang, X.-M. Lin, M. Sprung, S. Narayanan, J. Wang, Capturing the crystalline phase of two-dimensional nanocrystal superlattices in action. *Nano Lett.* **10**, 799–803 (2010).
- E. Josten, E. Wettterskog, A. Glavic, P. Boesecke, A. Feoktystov, E. Brauweiler-Reuters, U. Rücker, G. Salazar-Alvarez, T. Brückel, L. Bergström, Superlattice growth and rearrangement during evaporation-induced nanoparticle self-assembly. *Sci. Rep.* **7**, 2802 (2017).
- S. Maiti, A. André, R. Banerjee, J. Hagenlocher, O. Konovalov, F. Schreiber, M. Scheele, Monitoring self-assembly and ligand exchange of PbS nanocrystal superlattices at the liquid/air interface in real time. *J. Phys. Chem. Lett.* **9**, 739–744 (2018).
- S. Narayanan, J. Wang, X.-M. Lin, Dynamical self-assembly of nanocrystal superlattices during colloidal droplet evaporation by in situ small angle X-ray scattering. *Phys. Rev. Lett.* **93**, 135503 (2004).
- L. Wu, J. J. Willis, I. S. McKay, B. T. Diroll, J. Qin, M. Cargnello, C. J. Tassone, High-temperature crystallization of nanocrystals into three-dimensional superlattices. *Nature* **548**, 197–201 (2017).
- R. P. A. Dullens, E. M. Claesson, W. K. Kegel, Preparation and properties of cross-linked fluorescent poly(methyl methacrylate) latex colloids. *Langmuir* **20**, 658–664 (2004).
- U. Gasser, E. R. Weeks, A. Schofield, P. N. Pusey, D. A. Weitz, Real-space imaging of nucleation and growth in colloidal crystallization. *Science* **292**, 258–262 (2001).
- C. Noirjean, M. Marcellini, S. Deville, T. E. Kodger, C. Monteux, Dynamics and ordering of weakly Brownian particles in directional drying. *Phys. Rev. Mater.* **1**, 065601 (2017).
- N. de Jonge, L. Houben, R. E. Dunin-Borkowski, F. M. Ross, Resolution and aberration correction in liquid cell transmission electron microscopy. *Nat. Rev. Mater.* **4**, 61–78 (2019).
- N. de Jonge, Theory of the spatial resolution of (scanning) transmission electron microscopy in liquid water or ice layers. *Ultramicroscopy* **187**, 113–125 (2018).
- S. Mourdikoudis, L. M. Liz-Marzán, Oleylamine in nanoparticle synthesis. *Chem. Mater.* **25**, 1465–1476 (2013).
- T. Kister, D. Monego, P. Mulvaney, A. Widmer-Cooper, T. Kraus, Colloidal stability of apolar nanoparticles: The role of particle size and ligand shell structure. *ACS Nano* **12**, 5969–5977 (2018).
- J. Hermannsdörfer, N. de Jonge, Studying dynamic processes of nano-sized objects in liquid using scanning transmission electron microscopy. *J. Vis. Exp.* **2017**, e54943 (2017).
- G. Ge, L. Brus, Evidence for spinodal phase separation in two-dimensional nanocrystal self-assembly. *J. Phys. Chem. B* **104**, 9573–9575 (2000).
- H. C. Williams, Tilings and patterns, by B. Grünbaum and G. C. Shephard. Pp 700. £54.95. ISBN 0-7167-1193-1 (hardback) (Freeman). *Math. Gazette* **71**, 347–348 (1987).
- T. Dotera, S. Bekku, P. Ziherl, Bronze-mean hexagonal quasicrystal. *Nat. Mater.* **16**, 987–992 (2017).
- M. Elimelech, *Particle Deposition and Aggregation: Measurement, Modeling and Simulation* (Butterworth Heinemann, 2004).
- E. Abe, Y. F. Yan, S. J. Pennycook, Quasicrystals as cluster aggregates. *Nat. Mater.* **3**, 759–767 (2004).
- M. Zobel, R. B. Neder, S. A. J. Kimber, Universal solvent restructuring induced by colloidal nanoparticles. *Science* **347**, 292–294 (2015).
- D. Monego, T. Kister, N. Kirkwood, P. Mulvaney, A. Widmer-Cooper, T. Kraus, Colloidal stability of apolar nanoparticles: Role of ligand length. *Langmuir* **34**, 12982–12989 (2018).
- C. Wohlfahrt, *Landolt-Börnstein—Group IV Physical Chemistry* (Springer, 2008).
- L. Reimer, H. Kohl, *Transmission Electron Microscopy: Physics of Image Formation* (Springer, 2008).

Acknowledgments: We thank M. Koch and P. Kunnas for help with electron microscopy, S. Smolka for help with the figures, and E. Arzt for support through INM. **Funding:** The authors acknowledge that they received no funding in support of this research. **Author contributions:** All authors designed the experiments and contributed to the writing of the manuscript. E.C.-P. and D.D. conducted experiments and analyzed data. **Competing interests:** The authors declare that they have no competing interest. **Data and materials availability:** All data needed to evaluate the conclusions in the paper are present in the paper and/or the Supplementary Materials. Additional data related to this paper may be requested from the authors.

Submitted 8 November 2019

Accepted 28 February 2020

Published 13 May 2020

10.1126/sciadv.aba1404

Citation: E. Cepeda-Perez, D. Doblas, T. Kraus, N. de Jonge, Electron microscopy of nanoparticle superlattice formation at a solid–liquid interface in nonpolar liquids. *Sci. Adv.* **6**, eaba1404 (2020).

Electron microscopy of nanoparticle superlattice formation at a solid-liquid interface in nonpolar liquids

E. Cepeda-Perez, D. Doblas, T. Kraus and N. de Jonge

Sci Adv **6** (20), eaba1404.
DOI: 10.1126/sciadv.aba1404

ARTICLE TOOLS	http://advances.sciencemag.org/content/6/20/eaba1404
SUPPLEMENTARY MATERIALS	http://advances.sciencemag.org/content/suppl/2020/05/11/6.20.eaba1404.DC1
REFERENCES	This article cites 34 articles, 4 of which you can access for free http://advances.sciencemag.org/content/6/20/eaba1404#BIBL
PERMISSIONS	http://www.sciencemag.org/help/reprints-and-permissions

Use of this article is subject to the [Terms of Service](#)

Science Advances (ISSN 2375-2548) is published by the American Association for the Advancement of Science, 1200 New York Avenue NW, Washington, DC 20005. The title *Science Advances* is a registered trademark of AAAS.

Copyright © 2020 The Authors, some rights reserved; exclusive licensee American Association for the Advancement of Science. No claim to original U.S. Government Works. Distributed under a Creative Commons Attribution NonCommercial License 4.0 (CC BY-NC).